AeroBest 2023
Lisboa, 19-21 July 2023

WING STRUCTURAL DESIGN FOR A MAME UAV USING HIGH-FIDELITY NUMERICAL TOOLS

Vítor M. T. Silva[1], Nuno M. B. Matos[2] and André C. Marta[1]

1:IDMEC
Instituto Superior Técnico
Universidade de Lisboa
Av. Rovisco Pais, 1, 1049-001 Lisboa, Portugal
{vitortavaressilva8,andre.marta}@tecnico.ulisboa.pt, http://mdo.tecnico.ulisboa.pt

2: Research and Development
Tekever UAS
Tekever
2500-750 Caldas da Rainha
nuno.matos@tekever.com, http://www.tekever.com

Abstract. *With the rapid growth of the UAV market, the search for more efficient solutions promotes a huge competitive advantage for manufacturers. With the implementation of optimization techniques and the use of high-fidelity analysis in aircraft design, it is possible to develop better solutions. This work addresses the desire of a leading UAV manufacturer to improve its fleet to remain competitive in the surveillance UAV market. For this, a structural analysis tool using the finite element method is demonstrated, which is then used as part of a structural optimization framework. For this demonstration, static analyses of the wingbox of an existing UAV model, with a CFRP material with different lay-ups in certain areas of the model, are carried out for cruise and 4g load case, obtaining results of deformation and failure of this wing. These results help to identify possible weaknesses of the wing, as well as evaluate how the wingbox structural behaviour changes. The goals of this work include the validation of the numerical design framework using available experimental data and the study of alternative wing structural solutions. The results of the experimental and computational analyses presented slight differences. This was the expected behaviour due to model simplifications, which allowed for the the framework to be validated and proven useful. Three new optimal wingbox solutions were found, having a theoretical mass reduction of about 50%, while respecting a safety factor of 1.5. The first was optimised without displacement constraints and the other two had a maximum allowed displacement. These two differ on the optimization starting point to check for possible local minima, which were found.*

Keywords: optimization, design framework, adjoint method, finite element method, composite materials, fiber orientation

1 INTRODUCTION

With the continuous development and technological improvements of the Unmanned Aerial Vehicles (UAV) industry, different sizes and configurations were found useful to cover a wide range of missions. Nowadays, these vehicles are equipped with various electronic equipment, such as different cameras and sensors, depending on their intended purpose, and turning these in highly complex systems. Some use cases of these Unmanned Aerial Systems (UAS) and their advantages include: inspection of photovoltaic plants, to reduce the time of manual inspections [1]; precision agriculture, for weed mapping and management, vegetation health and growth monitoring, irrigation management and crops spraying [2]; urban environment and management, to give real-time monitoring of traffic, road conditions as well as building observation [3]; disaster hazard and rescue, to quickly and accurately respond when necessary as well as post-disaster assessment and emergency response in remote places; and maritime monitoring, to control oil spills, gas pipes, whales and marine life, tracking fishing boats as well as controlling illegal immigration.

Various applications have been brought up and many more are yet to be developed. Investments in the UAS industry have been a trend for the past couple of years, with many companies, mainly start-ups, directing their funds to explore new and original applications to be competitive. Since 2000, more than 300 start-ups entered the UAS market, focusing on hardware, support services and operations [4]. They have gathered more than 3 billion USD to develop the industry with new applications.

In order to remain competitive in this growing market, the demand for highly efficient and optimized UASs increases.

2 TEKEVER'S AR5 UAS

Tekever is a company founded in 2001 that manufactures and operates their UAS mainly for surveillance missions. An objective was set to optimize their most advanced Medium Altitude Medium Endurance (MAME) UAS - the AR5 (Fig. 1) - using high-fidelity tools. This paper is the starting point of this project, introducing the numerical tools and proving the concept.

Figure 1: Tekever AR5

The main AR5 specifications are resumed in Tab. 1.

For take-off and landing specifications, this UAS needs a track. As a drawback, it can not take-off with crosswinds. Regarding the payload, one advantage is that, for rescue

Table 1: Some characteristics of the Tekever's AR5 [5]

Wing span	Cruise speed	MTOW	Payload capacity	Endurance	Communications range
7.3 m	100 km h^{-1}	180 kg	50 kg	12 h*	Unlimited (SATCOM)

* Expected endurance with inflating raft

missions, that may require fast action on site, the AR5 can transport an inflating raft. However, this added weight might affect the total endurance, and reduce total operating time from 16h to 12h. Finally, since it uses Satellite Communication (SATCOM) for communication with the operator, there is no range limit for operating, which is really advantageous.

Since the performance evaluation of the configuration come usually from estimations with empiric correlations, very simplified calculus or, in later stages, computational solid mechanics (CSM) for a structural case, it would benefit from the creation of some automated steps. In [6], Grose explains that the competitiveness of a company is high if: it can provide fast responses to consumer needs by reducing development or manufacturing times; the aircraft is produced with the least possible costs; and if it requires low maintenance, indicating a good final product quality. Using optimization as a tool to improve in all these aspects, the design traditional process can be adapted by having an optimizer directly and automatically changing some pre-established design variables. By combining this with a judgment of an experienced engineer, the final product should also have a superior quality.

3 STRUCTURAL ANALYSIS AND OPTIMIZATION

3.1 Finite Element Method

For the structural analysis presented in this paper, the FEM method is used due to its high capabilities of modelling complex geometries and its high use in the aeronautic industry for structural applications.

For thin structures, like the wing's skin, 2D shell elements are used to model the middle plane of the skin [7].

In this work, the elements used in the analysis are the 4-node quadrangular elements based on a Mixed-Interpolation of Tensorial Components (MITC) approach, which avoid shear and membrane locking [8, 9]. It is important to note that a modelling error is introduced which makes these not suitable for shell structures with high thickness and curvature radius.

For these elements, the basis theory is the classical first order deformation theory [9]. In this, the transverse plane does not remain perpendicular to the mid plane after deformation including shear strains in model. With it, the variables to be determined in this formulation are the mid-plane displacements and the rotations about the x and y axis. To add the rotation about z (also called "drilling degree of freedom"), a penalty approach is used [10, 11]. Then, with laminate constitutive equations, the stresses are obtained from the strains.

3.2 Material Characterization and Modelling

The structures to be analysed are composed of Carbon Fiber Reinforced Polymer (CFRP) plies that, when stacked, form the laminate. Since each ply is composed of unidirectional fibers in a matrix medium, it presents an orthotropic behaviour, with 9 independent properties that define this material constitutive law:

$$\begin{Bmatrix} \varepsilon_1 \\ \varepsilon_2 \\ \varepsilon_3 \\ \varepsilon_4 \\ \varepsilon_5 \\ \varepsilon_6 \end{Bmatrix} = \begin{bmatrix} \frac{1}{E_1} & -\frac{\nu_{21}}{E_2} & -\frac{\nu_{31}}{E_3} & 0 & 0 & 0 \\ -\frac{\nu_{12}}{E_1} & \frac{1}{E_2} & -\frac{\nu_{32}}{E_3} & 0 & 0 & 0 \\ -\frac{\nu_{13}}{E_1} & -\frac{\nu_{23}}{E_2} & \frac{1}{E_3} & 0 & 0 & 0 \\ 0 & 0 & 0 & \frac{1}{G_{23}} & 0 & 0 \\ 0 & 0 & 0 & 0 & \frac{1}{G_{13}} & 0 \\ 0 & 0 & 0 & 0 & 0 & \frac{1}{G_{12}} \end{bmatrix} \begin{Bmatrix} \sigma_1 \\ \sigma_2 \\ \sigma_3 \\ \sigma_4 \\ \sigma_5 \\ \sigma_6 \end{Bmatrix} \tag{1}$$

with E_i as the Young's Modulus for the ith direction, ν_{ij} as the ratio between transverse shear in the jth direction to the axial strain in the ith direction with an applied stress in the ith direction (Poisson's ratio) and G_{ij} as the shear modulus for the ijth plane [9].

To model the composite material that composes the wingbox, a smeared approach is used [12]. This method describes the composite structure using fractions of plies (f_{θ_i}) and their respective angles (θ_i) It is necessary to provide the elastic and strength properties of each ply as well as the total thickness of the laminate. With these, the global stiffness matrix is weighted with each ply fraction of a certain orientation. A visual diagram of the geometric parameters necessary for this model is presented in Fig. 2.

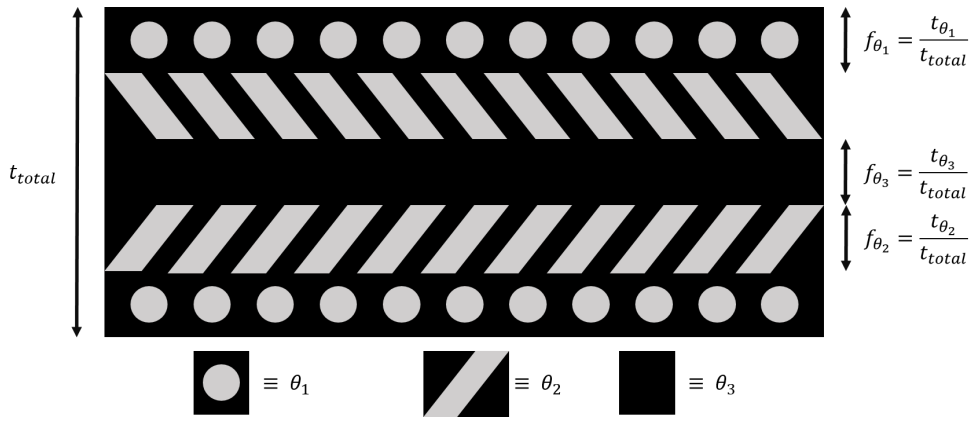

Figure 2: Composite representation with the necessary parameters to define the smeared model

To predict failure of composite materials, it is necessary to characterize the composite strength for different load conditions (axial, transverse and shear tensile stresses), which are reflected in their longitudinal, transverse and shear tensile strength parameters.

In this work, the *Tsai-Wu* Criterion is used and defined as

$$F_{TW} = F_1\sigma_1 + F_2\sigma_2 + F_{11}\sigma_1^2 + 2F_{12}\sigma_1\sigma_2 + F_{22}\sigma_2^2 + F_{66}\sigma_{12}^2 \ , \tag{2}$$

where σ_i is the stress component in the ith direction in the principal material coordinates of each ply (1 to 3 are normal stresses and 4 to 6 shear stresses) and F_{ij} are coefficients depending on the material normal and shear strengths [9]. Note that, when this F_{TW}

failure index is equal or above 1, material failure is expected and no stress components are present in the 3rd direction of space since the shell elements assume that $\sigma_z = \sigma_3 = 0$.

3.3 Optimization Techniques

The general structural optimization problem can be stated as

$$\begin{array}{ll} \text{Minimize} & f(v, u_1, ..., u_{n_l}) \\ \text{w.r.t.} & v, u_1, ..., u_{n_l} \\ \text{governed by} & R_i(X^N(v_G), v_M, u_i) = 0 \\ \text{subject to} & g_i(v, u_i) \leq 1 \end{array} \tag{3}$$

where $f(v, u_1, ..., u_{n_l})$ is the objective function, $g_i(v, u_i)$ is a constraint vector for the ith load case, up to a total of n_l, $x = (v_G, v_M)$ are the design variables, divided as geometric and material design variables, respectively, $X^N(v_G)$ are the nodal locations, u_i are the state variables for the ith load case and R_i are the finite-element residuals.

to compute gradients, either of the objective function or the constraint functions with respect to the design variables. These are very computationally expensive to calculate and many methods have been developed to make them more efficient to compute. Kennedy & Martins [13] and Kenway et al. [14], for example, used a gradient-based algorithm for an aerostructural optimization of a wing and a wide-body transport aircraft, respectively, due to the large number of design variables (thousands). The most important aspect in these cases was that the derivatives were obtained by the adjoint method. Another use for this type of gradient-based methods is given by Werter & De Breuker [15] by using a globally convergent method of moving asymptotes (GCMMA) to minimize a wing weight with respect to some lamination parameters and the laminate thickness. One of the key aspects in this case was that the derivatives were obtained using the direct method and with the use of analytically obtained sensitivities of the objective and constraints' functions with respect to the design variables.

In the context of this work, the gradient-based optimization seems the most favourable approach since the number of design variables is high and the functions of interest are smooth. One of the most commonly used approaches to solve the optimization problem is recurring to a sequential quadratic programming method. One great example is the Sequential Least Squares Quadratic Programming method (SLSQP) which uses the Han–Powell quasi-Newton method with a BFGS update of the B-matrix and an L1-test function in the step-length algorithm [16]. This method approximates the Lagrangian to a quadratic function and linearizes both equality and inequality constraints [16, 17]. A studied performed by Zhoujie et al. [18] showed that, for a multi-dimensional Rosenbrock function, the SLSQP algorithm performed the best among several other gradient-based and -free methods, converging the fastest, with the least amount of function evaluations. Not only that, but both this algorithm and the Sparse Nonlinear Optimizer (SNOPT) performed the greatest when obtaining the minimum C_D when changing the wing twist or shape. This results were especially good using the adjoint method for the derivatives. This SLSQP method is commonly used in aerodynamic shape optimization [19, 20], airfoil shape optimization problems [21] as well as aerostructural problems [22].

3.3.1 Adjoint Method

To compute gradients, either of the objective function or the constraint functions with respect to the design variables, the chosen method and the one used by the optimization framework, is the adjoint method. Since these gradients are very computationally expensive to calculate, many methods have been developed to make them more efficient to compute. Kennedy & Martins [13] and Kenway et al. [14], for example, used a gradient-based algorithm for an aerostructural optimization of a wing and a wide-body transport aircraft, respectively, due to the large number of design variables (thousands), which is bigger than the number of constraints' functions. On the other hand, if the situation was the opposite, the direct method used by Werter & De Breuker [15] to minimize a wing weight with respect to some lamination parameters and the laminate thickness, would be the most efficient. One of the other key aspects, besides the use of the direct method in this case, was the use of analytically obtained sensitivities of the objective and constraints' functions with respect to the design variables that help gradient-based optimizations to be faster.

The derivatives of an objective function f and the residual of the governing equation $R(x_n, y_i(x_n))$ can be given by the chain rule as

$$\begin{aligned} \tfrac{df}{dx_n} &= \tfrac{\partial f}{\partial x_n} + \tfrac{\partial f}{\partial y_i}\tfrac{dy_i}{dx_n} \\ \tfrac{dR}{dx_n} &= \tfrac{\partial R}{\partial x_n} + \tfrac{\partial R}{\partial y_i}\tfrac{dy_i}{dx_n} = 0 \, . \end{aligned} \tag{4}$$

where x_n are the design variables and y_i the state variables. Using a reduced-space (or nested) approach [23] to the problem, the structural analysis of the model is solved repeatedly in each optimisation iteration. This means that the derivatives in Eq. (4) are necessary in each iteration. With variational calculus, the partial derivatives from the first expression can be easily obtained. However, the total derivative $\frac{dy_i}{dx_n}$ is computationally expensive since it requires solving the structural model, after imposing a small perturbation in x_n, to obtain y_i. To tackle this problem of solving the total derivatives, the derivative of the residuals in Eq. (4) can be re-written as

$$\frac{\partial R}{\partial y_i}\frac{dy_i}{dx_n} = -\frac{\partial R}{\partial x_n} \Leftrightarrow \frac{dy_i}{dx_n} = -\left[\frac{\partial R}{\partial y_i}\right]^{-1}\frac{\partial R}{\partial x_n} \, . \tag{5}$$

Replacing this in Eq. (4) of the function f,

$$\frac{df}{dx_n} = \frac{\partial f}{\partial x_n} + \frac{\partial f}{\partial y_i}\left[\frac{\partial R}{\partial y_i}\right]^{-1}\frac{\partial R}{\partial x_n} \, . \tag{6}$$

Using

$$\psi^T \equiv \frac{\partial f}{\partial y_i}\left[\frac{\partial R}{\partial y_i}\right]^{-1} \tag{7}$$

$$\left[\frac{\partial R}{\partial y_i}\right]^T \psi = \frac{\partial f}{\partial y_i}^T \tag{8}$$

where ψ is called the adjoint vector. Solving the equivalent Eq. (8), also called adjoint equation, to obtain ψ, it can then be replaced in Eq. (5) and the derivative of the function f found. This procedure to compute derivatives is called the adjoint method. From Eq.

(8), it is possible to conclude that in order to obtain the adjoint vector, this equation needs to be solved as many times as the number of functions f that there are in the optimisation problem. So, this problem complexity scales with the number of functions.

3.4 CSM Analyses' Steps and TACS Framework

From the CAD file containing the geometry information of the wingbox to be evaluated up to the output results of the finite element analysis, and the posterior optimization, a sequence of steps need to be followed and different software used, as presented in Fig. 3.

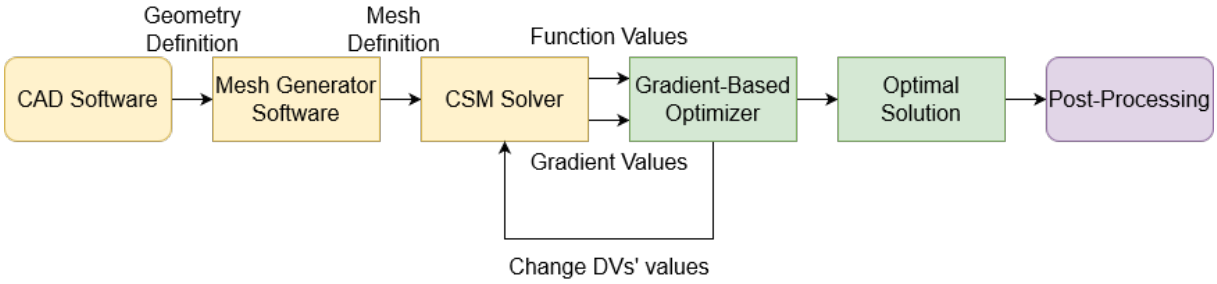

Figure 3: Flowchart of the structural optimization framework with highlight in yellow of the structural analysis components

Firstly, the geometry defined in the CAD needs to be exported as a file with a specific compatible format to be read by a mesh generator software. This geometry definition file contains information about the nodes location, elements identification and nodes which define them and the type of elements used. This is fed into the CSM software so that the finite element model can be used with that discretization.

The CSM software used is TACS [8], an open-source FEM solver. In TACS, load cases are set to condition the problem before it is solved and boundary conditions imported from the mesh definition file. In every problem iteration, the TACS software gives function values and gradients to a gradient-based optimizer, which then iterates until the optimum solution for the intended problem is found. A flow chart representing the TACS workflow is presented in Fig. 4.

4 WING STRUCTURE ANALYSIS

4.1 AR5 Wing Definition

The baseline and start of the optimisation process of the AR5 is its wing, since it is the main component of the UAV. The wingbox can be parametrized in several ways. To do this, some groups within the structure are created, sharing the same parameters, to later, in the optimization process, these varying equally within the group. In Fig. 5 the groups can be observed in different colours as well as the internal wingbox structure and reference frame used throughout its analysis. The parameters that define each group are total thickness, type of materials, their proportions and the ply angles (parameters from Fig. 2).

The AR5 wingbox is composed sandwich composite components with different thicknesses and fractions of core and shell material. A representation of these sandwich components is shown in Fig. 6.

The core consists on a low weight rigid foam which gives the necessary stiffness to

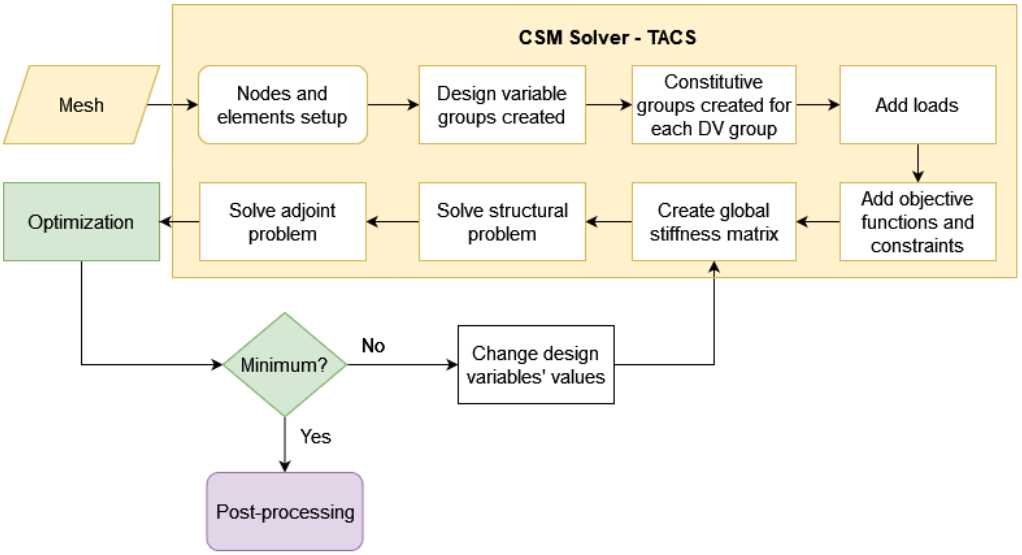

Figure 4: Flow chart of the steps to solve an optimization problem

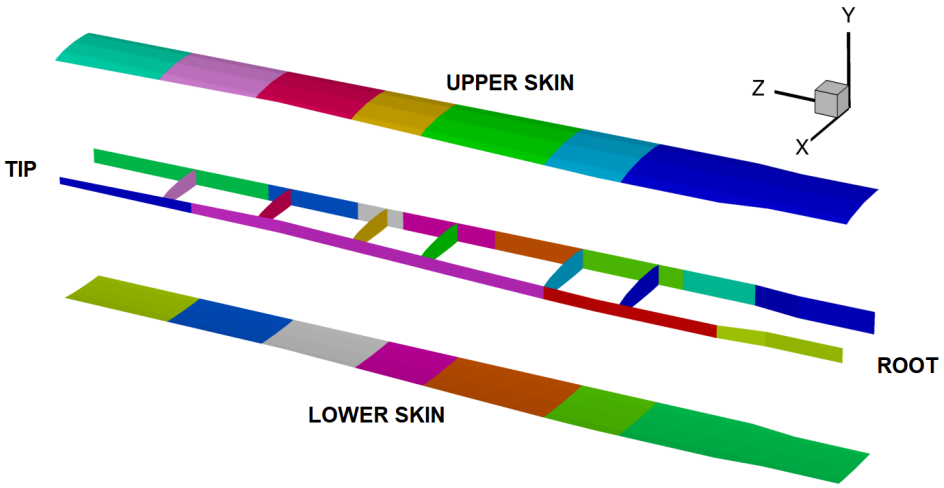

Figure 5: Representation of the design variable groups

the wing, with very low weight. Different versions and proportions of this core are used depending on the wingbox section and a detailed description cannot be provided due to confidentiality restrictions. The physical and mechanical properties used are summarized in Tab. 2. It is important to note that, only the in-plane properties were the necessary manufacturer's properties since in the shell formulation, the transverse strain in neglected. This means that, since the foam core properties in-plane are independent of direction, this material can be modelled as isotropic.

Table 2: Foam core properties

Density
Tensile modulus in the plane
Shear modulus
Tensile strength in the plane

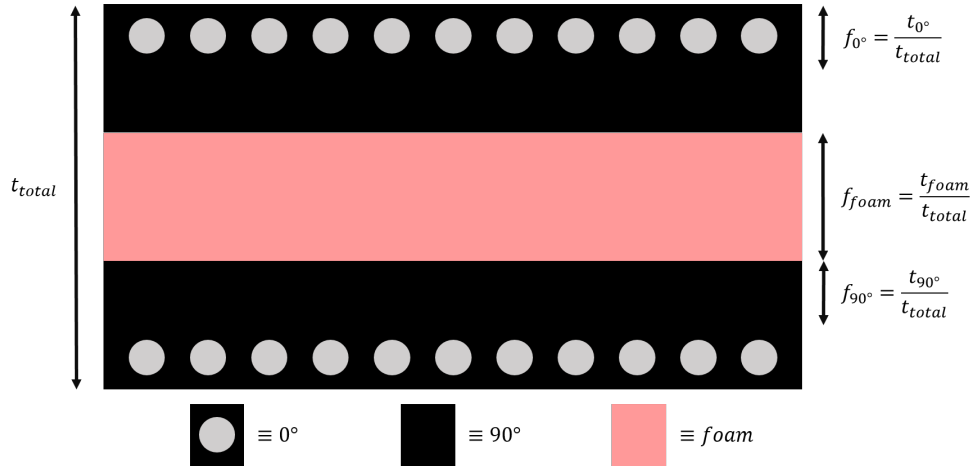

Figure 6: Representation of the sandwich composite (CFRP with black matrix and grey fibers and foam core foam in pink)

Table 3: Density and physical properties of CFRP ply

Density*
Young's modulus (Fiber Direction)*
Young's modulus (Transverse Direction)*
Shear modulus
Poisson ratio
Tensile strength (Fiber Direction)
Compressive strength (Fiber Direction)
Tensile and compressive strength (Transverse Direction)
Shear strength

* Obtained from rule of mixtures

For the shell, a CFRP layup is used with plies of 0° and 90° as a starting point.A summary of the properties obtained can be seen in Tab. 3.

To define the material composed of both the foam and CFRP, present in the wingbox, the constitutive model explained in 3.2 is used. In TACS, however, a complete and detailed model of this material is not possible, mainly due to the fact that the core is fully enclosed by the CFRP, in contrast with the layup in Fig. 6 and some properties are not exactly representing the real material. These are the major limitations in terms of material that were encountered and a probable cause for different results between a real test and a computational analysis. Nonetheless, the analysis is performed and an optimization can be carried out later, based on this.

Finally, to acknowledge the possible differences between the mass calculated from the structural model and the real mass of each component, measured by the Tekever's quality control team, the error of the model relative to the measured values is given in Tab. 4.

Table 4: Error of model mass relative to measured mass of AR5 wingbox components

	Lower Skin	Upper Skin	Spars	Ribs	Total
Model to real difference [%]	+19.1*	+26.1*	-30.9	-50.0	-1.7

* Extrapolated value

It is possible to observe that, the calculated total mass is slightly underestimated in the model. Firstly, for the skin mass, an estimation was needed to compare the real and model values since due to the simplifications needed for the wingbox meshing, the skin panels that are computed are only present between the spars. So, with those panel's mass, an extrapolation was made to obtain the estimated weight of the real model skin and it is shown in Tab. 4. This extrapolation was simply made considering the chordwise position of the spars and would be accurate if the skin panels were straight and parallel to the chordwise direction. Since there are a few geometric or material properties' differences, some discrepancies are present in the model. For example, spar's beam profile in the model is simply rectangular, however, in reality, this is not the case. This means that a good amount of material is not considered hence, resulting in a underestimation of the mass in the model. Finally, it is important to note that, overall, the difference is not high (about 2% error) and does not affect the wing's rigidity directly.

4.2 Mesh Convergence Study

Some model simplifications and limitations were encountered Nonetheless, the structure is composed by 6 ribs, 2 spars and the skin panels between these. The simplifications include the trimming of the ribs' leading edge at the front spar, the addition of a rear spar section close to the tip and the skin panels are only present, between the spars (no leading or trailing edge skin panels).

To decide on the mesh refinement level, a mesh convergence study was carried out with 5 meshes, as summarized in Tab. 5. A representation of mesh 1 can be seen in Fig. 7 were the others are a subdivision of this one, where each element is divided by 4 (except number 5 due to a memory error that could not be resolved).

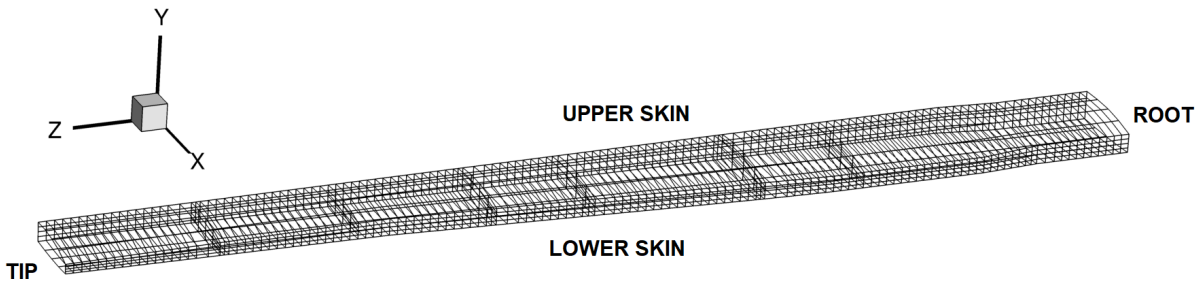

Figure 7: Mesh of the AR5 wingbox

Table 5: Convergence study

Mesh	Number of elements	Degrees of freedom	Max disp. (Tip Rear Spar - USkin) [mm]	Diff.	Stress (Root Front Spar - LSkin) [Pa]	Diff.	RAM [GB]	Time [s]
#1	2,272	13,476	0.274	-	60,490	-	0.1	30
#2	9,088	54,180	0.273	0.15%	62,450	-3.14%	0.3	238
#3	36,352	217,380	0.273	-0.09%	64,280	-2.85%	1.0	378
#4	145,408	870,948	0.266	2.60%	66,089	-2.74%	4.9	410
#5	284,672	1,706,532	0.266	-0.01%	66,753	-1.00%	8.8	466

To choose the most efficient mesh to obtain the structural results from and use during the optimization process, the criteria was: it had to be converged, so a deviation on the monitored values between meshes shouldn't be above one percent; and it should be the one that takes the least time and memory to solve. Looking at the Tab. 5, it was concluded that mesh 4 met all criteria.

As a final regard, these results were obtained with a computer using a 16-core processor with 4.5 GHz base frequency and 128 GB of RAM.

4.3 Design Framework Validation

To validate this numerical design framework, experimental data was used from a static wing bending test provided by Tekever. Weights were added in the lower skin with the wing upside down and the tip displacement measured.

Analysing with TACS, the maximum deflection obtained was about 0.17 m across the tip. The original and deformed shapes can be observed in Fig. 8.

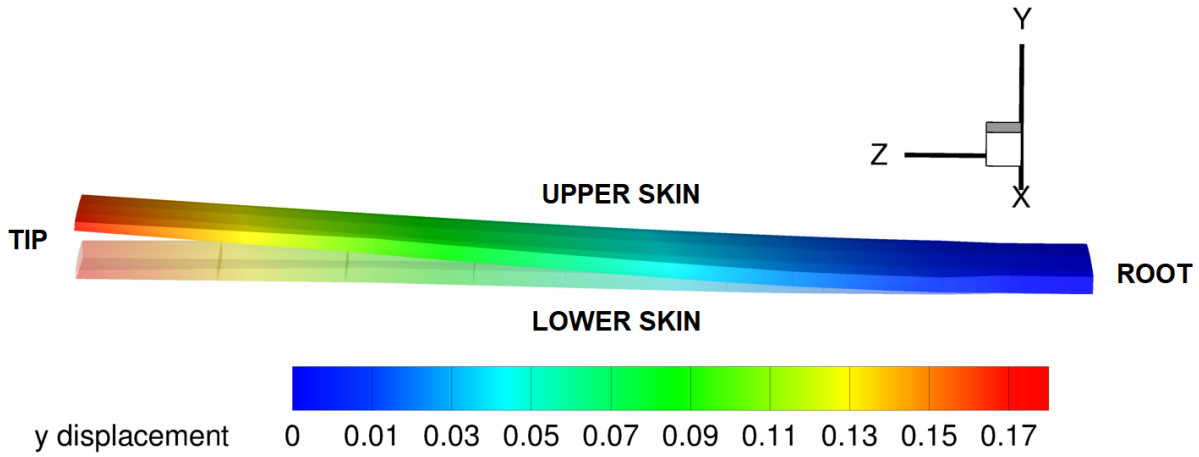

Figure 8: Wingbox's displacement in y under the fixed loads condition

According to the ground test values, the measured displacements, at the tip, for the leading edge and trailing edge were 0.12 m and 0.17 m, respectively. Firstly, the order of magnitude of the computational results is pretty similar which is a good indicator that the model is behaving as expected. Secondly, the fact that there is no significant difference between the leading and trailing edge from the computational results is due to the spar section close to the tip not existing in reality, so the trailing edge has lower stiffness and a higher displacement in the bending test. Finally, the computational results reproduce overall an higher displacement and this is the expected behaviour since, with the geometry approximations explained in Sec. 4.2 to produce the mesh, some wing elements were not added, making the wing less stiff and have a larger deformation. It can be concluded that the framework produced valid and coherent results.

4.4 Analysis of 4g Maneuvre

Since the maximum allowed loads within the flight envelope of the AR5 is a 4.0g maneuvre, this is the case studied. For this condition, the most important results to gather are the failure index and displacement, to make sure it is an acceptable amount.

The failure index results are shown in Fig. 9. They are satisfactory and well bellow

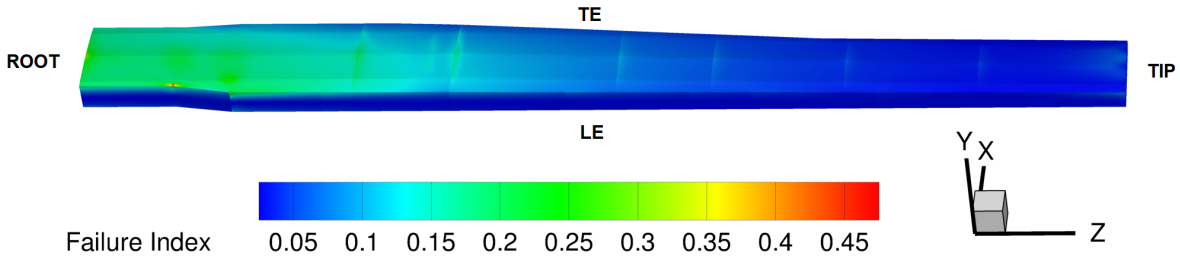

Figure 9: Wingbox failure index under the 4.0g condition

unity, being the maximum observed of 0.47 meaning that the structure has a safety factor of 2.1 and a large margin for improvement.

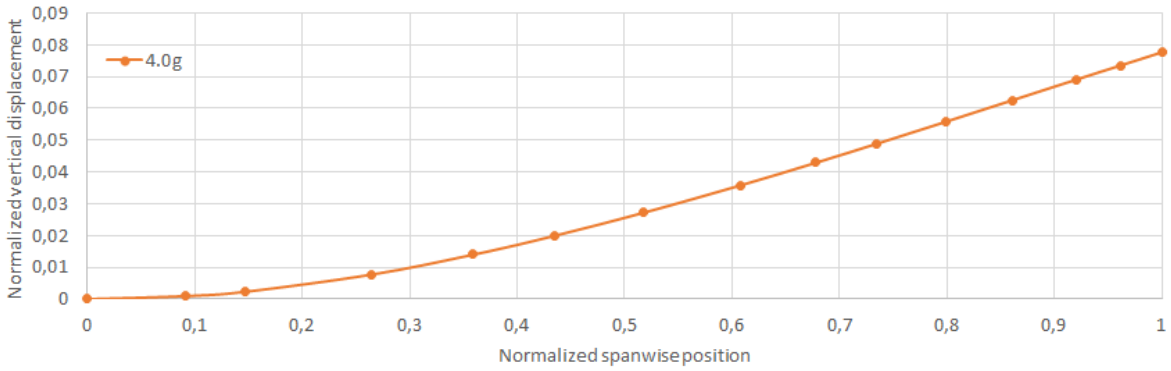

Figure 10: Vertical displacement at the front spar

Regarding the normalized vertical displacement that was plotted across the wingbox front spar in Fig. 10, the maximum obtained at the tip corresponds to about 8% of half span (0.264 m). This indicates that the deflection is not too large relative to the wing size and it is acceptable.

5 WING STRUCTURAL OPTIMIZATION

5.1 Baseline Problem Formulation

Tekever's goal is to minimize the structural mass and increase the efficiency of the AR5, meaning that the objective function to this problem is the total wingbox mass. This includes the ribs, spars and upper and lower skin,

$$m_{\text{total}} = m_{\text{ribs}} + m_{\text{spars}} + m_{\text{upper skin}} + m_{\text{lower skin}} \tag{9}$$

To control this mass, the variables allowed are some of the parameters that describe the wingbox design variable (DV) groups. In this case, the ones chosen are the thickness (t_i) of the ith DV group and the orientation (θ_{ij}) of the jth CFRP ply from the ith DV group. This last design variable does not have a direct impact on the weight but allows the wing to change is stiffness to possibly lower the thickness of the CFRP and still withstand the aerodynamic loads.

Some inequality constraints are set: adjacency constraints, to keep a thickness difference ($|t_i - t_k|$) between a certain ith DV group and its adjacent groups (kth DV groups)

under a certain maximum; failure constraints, in this case, the failure index given in Sec. 3.2 by the Tsai-Wu criterion, to ensure that the wing withstands the loads. Since it is not possible to obtain a gradient of a function that retrieves the maximum failure indexes across all points in which it is calculated, the Kreisselmeier-Steinhauser (KS) aggregation function [24] is used to convert the discrete nature of the maximum failure index function into a continuous and smooth function, allowing for a gradient-based optimizer to use it,

$$\mathrm{KS} = \frac{1}{\rho} \ln\left(\sum_{l=1}^{n_g} \exp(\rho g_l)\right) , \tag{10}$$

where ρ is a tolerance/weight parameter, n_g the number of failure constraints and g_l the lth failure constraint function.

With this in mind, the baseline optimization problem for this wingbox structure can be formulated as

$$\begin{array}{cc} \text{minimize} & m_{\text{total}} \\ \text{with respect to} & t_i \\ & \theta_{ij} \\ \text{subject to} & \mathrm{KS} \leq 1 \\ & |t_i - t_k| \leq \Delta_{max} \end{array} . \tag{11}$$

According to the manufacturing requirements and methods employed, the boundaries for each DV group is defined as: minimum of 1.0 mm for both skins and spars and 0.25 mm for the spars; to give more freedom to the optimizer to possibly reinforce certain areas of the wingbox, a maximum of 100 mm was set. For the adjacency constraint, Δ_{max} was defined as 5 mm.

The optimization algorithm used was the sequential least squares programming algorithm (SLSQP), briefly presented in Sec. 3.3. Convergence is assumed for the optimal solution when the difference between solutions is smaller than 10^{-6}. To ensure that the optimization process stops if no minimum is found and it does not run indefinitely, a maximum of 500 iterations are allowed.

5.2 Baseline Optimization

Fig. 11 shows the history of the objective and constraints in which the objective function exhibits a converging behaviour, reinforcing the fact that the optimisation found an optimal solution.

Another interesting aspect to note in Fig. 11 is the failure constraint has visible upper spikes that match with the mass lowering spikes, which happens when the optimiser tries to lower the mass, violating the failure constraint.

Fig. 12 compares the initial case with the found optimised solution having the different wingbox components' thicknesses. Across the entire wingbox, the thickness is lower in the optimal solution and, as expected, the higher and lower values are located near root and tip of the wing, respectively.

Regarding the failure index shown in Fig. 13, the optimised wingbox has more regions with a higher failure index, due to the overall decrease in the thickness and the wing being less oversized.

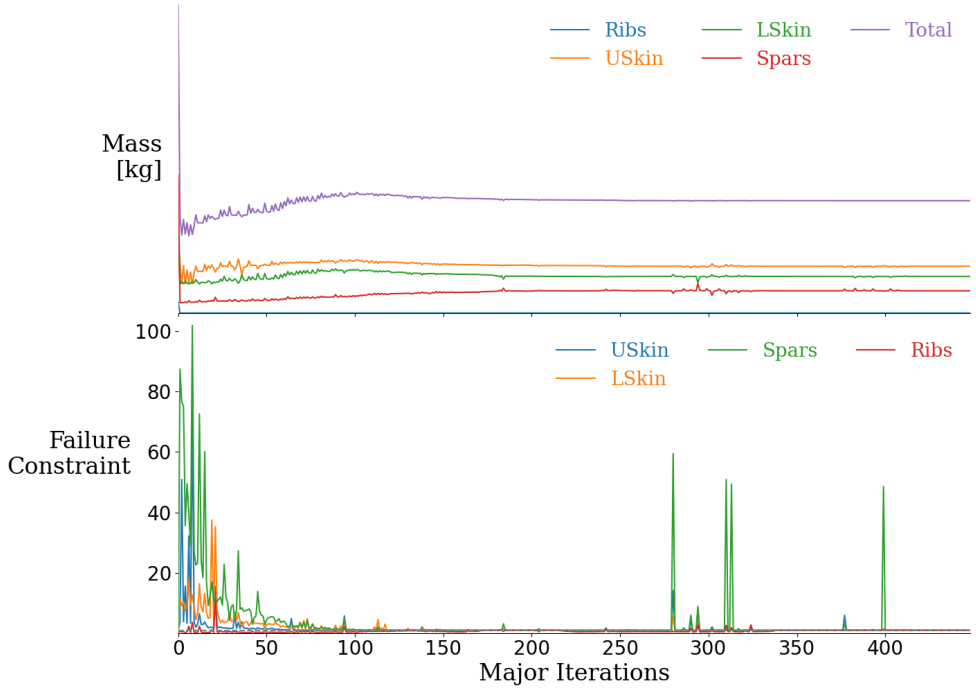

Figure 11: Objective function and failure constraint value across all optimization iterations

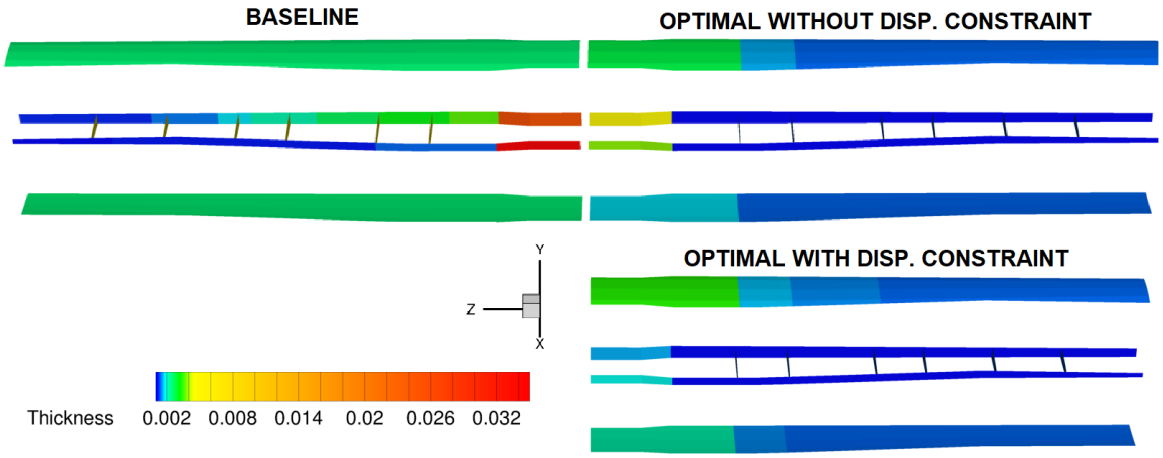

Figure 12: Comparison between initial component thicknesses (left) and optimised solution found (right)

With the thinning of the wingbox components and without buckling constraints present in this optimization, it is expected that the wing displacement increases. In fact, the optimized wingbox, for this 4g load condition, presents a maximum displacement of 0.61 m and its deformation is shown in Fig. 14.

5.3 Baseline Optimization with Displacement Constraint

To prevent such large displacement, another KS function, aggregating all displacements from a specific wingbox region is used, in order to more easily control the maximum displacement of that specific component. Similarly to the failure function, this displacement

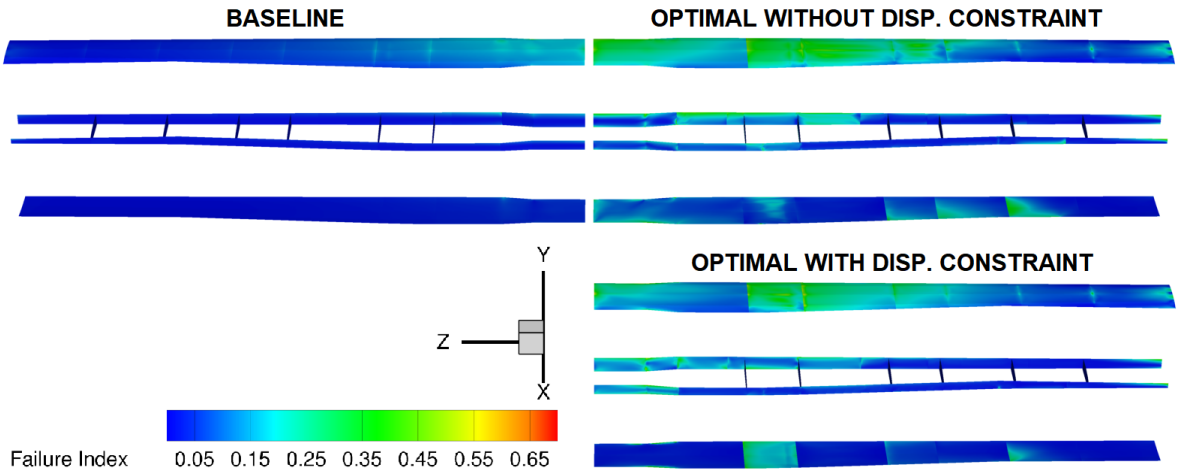

Figure 13: Comparison between initial component thicknesses (left) and optimised solution found (right)

constraint requires a KS function since the maximum function can not be differentiated. In the present case, the tip of the wing is the most problematic location so the constraining KS function uses the displacements in that region.

Having performed the optimization adding the inequality constraint, KS(disp) $< 0.4\,\mathrm{m}$, a similar plot to Fig. 11 was obtained, confirming convergence of the solution and constraints. By plotting the front spar normalized displacements against the spanwise position (Fig. 14) it is possible to assess that the constraint was successful at lowering the maximum allowed displacement.

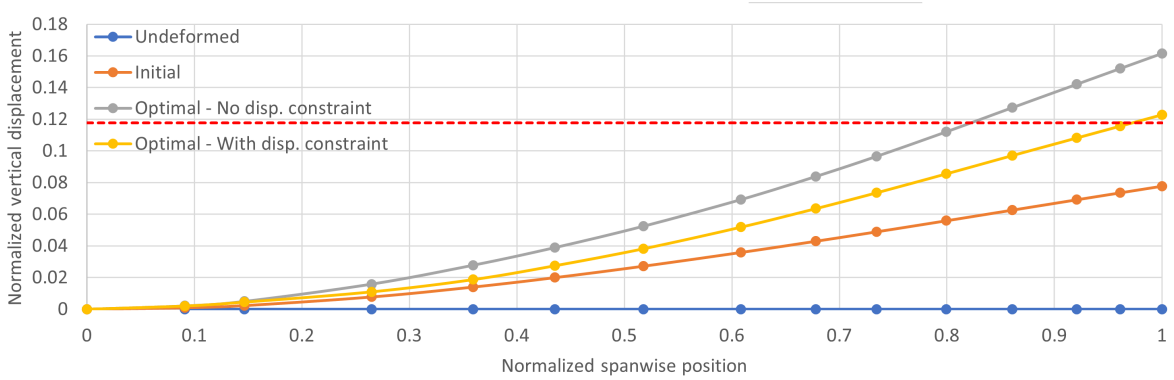

Figure 14: Front spar y deflection under the 4g condition

To ensure this new constraint was respected, it is interesting to see that, comparing the thickness of the components from previous optimal solution and the newer one (Fig. 12), the thickness increased, particularly near the root and for both the upper and lower skins. In contrast, there is a reduction in thickness near the root for both spars. This indicates that the root panels of the skin are more effective at increasing the wing bending stiffness and reducing the maximum displacement and it is possible to mitigate the weight gain by thinning the spars. Although making the spars thinner supposedly decreases their rigidity, the gain from the skin panels is greater and the overall weight is reduced this way.

From Fig. 13 and the information in Tab. 6, it is possible to conclude that the failure inequality constraint remained active, implying that the optimized structure under the 4g condition corresponds to the thinnest possible solution that still withstands the critical aerodynamic loads.

Using the optimal solution obtained from case 1 as the optimization starting point leads to a new solution, which corresponds to a different local minimum.

It is relevant to compare the results against the AR5 baseline analysis quantitatively, to better understand the enhancements these optimizations provide to the AR5 wing. In Tab. 6 is a summary of these results.

Table 6: Summary of relevant optimization results

	Mass difference	Maximum disp. [m]	Maximum failure index
Baseline	0%	0.273	0.47
Optimal - No disp. constraint	−55.6%	0.613	0.79
Optimal - With disp. constraint	−52.4%	0.473	0.74
Optimal - Different baseline	−54.4%	0.471	0.58

It is possible to conclude that these optimizations provide a mass reduction larger than 50% of the original baseline. As expected, with the displacement constraint, the reduction is smaller since, to increase the rigidity of the wing to respect the constraint, thicker sections were necessary. The third optimization case revealed to be important since by having the starting point as the optimal solution from the first optimization case, a better result could be found keeping the displacement constraint. The maximum displacement for the third solution was about 12% of the wing's half span, similar to the results in Fig. 14 for the second case, which is considered acceptable. Finally, regarding the possible wingbox failure, a safety factor of 1.5 was used so that all optimizations would have a maximum failure index of about $\frac{1}{1.5} = 0.67$. The third optimization is well within the limit having a maximum failure index of 0.58 and a 1.78 safety factor.

A full description of the final values of the design variables for each wingbox DV group is present in Tab. 7 for the three optimization cases (Case 1/Case 2/Case 3). The 0° ply orientation is defined by direction 1 of the local reference axis for each wingbox component: for both skins, spars and ribs, it corresponds to the z, y and x directions in Fig. 7, respectively.

It can be concluded that, across the span, the thickness decreases except for the rear spar although it is not too much (about 0.1 mm more than the previous panel). Furthermore, although the local minima produced a similar displacement response, it has a very distinct composition in terms of ply orientation, allowing the wingbox to satisfy the constraints with a higher safety factor (lower failure index).

Regarding the ribs, these are the parts that suffer the most thickness changes since their baseline value is 6 mm and, across all optimizations, the value is reduced to the minimum 1 mm. This might indicate that the baseline value is greatly oversized. Although it might be true, it cannot be concluded since no buckling constraints were added and the wingbox ribs main function is to increase the buckling strength.

One final note about the plies orientation and a main concern and physical constraint, is that if this wing was to be manufactured, since the angles of the different DV groups have large disparities between them, it would not be possible to manufacture it with unidirectional fiber cloths. Using them, would lead to non continuity of the fibers along

Table 7: Design variables' values of the optimal solutions

Upper Skin	1 (Root)	2	3	4	5	6	7 (Tip)
t [mm]	2.8/3.3/3.0	1.4/1.4/1.3	1.0/1.2/1.0	1.0/1.0/1.0	1.0/1.0/1.0	1.0/1.0/1.0	1.0/1.0/1.0
θ_1 [°]	-1.1/-7.8/-3.6	-1.4/-5.2/-2.6	-4.8/-2.4/-2.4	-20.1/-1.9/-3.6	3.0/-2.7/-1.9	-1.7/-1.7/-0.1	9.5/7.9/6.0
θ_2 [°]	90.0/19.6/90.0	90.0/27.8/90.0	32.8/90.0/-2.5	24.3/90.0/0.1	87.8/90.0/-0.6	88.1/90.0/90.0	87.9/90.0/90.0

Lower Skin	1 (Root)	2	3	4	5	6	7 (Tip)
t [mm]	1.7/2.2/2.1	1.0/1.2/1.0	1.0/1.0/1.0	1.0/1.0/1.0	1.0/1.0/1.0	1.0/1.0/1.0	1.0/1.0/1.0
θ_1 [°]	-1.8/-5.7/-5.3	-14.4/3.2/-16.3	-4.1/-8.5/10.3	7.9/1.3/3.5	16.6/0.7/6.3	43.2/30.5/-21.4	52.5/58.4/62.8
θ_2 [°]	56.8/14.0/18.0	22.0/90.0/19.6	20.8/13.8/-4.6	84.9/89.7/-0.3	89.9/77.4/-4.3	90.0/90.0/19.8	52.5/58.3/63.2

Ribs	1 (Closer to root)	2	3	4	5	6 (Closer to tip)
t [mm]	1.0/1.0/1.0	1.0/1.0/1.0	1.0/1.0/1.0	1.0/1.0/1.0	1.0/1.0/1.0	1.0/1.0/1.0
θ_1 [°]	-17.3/-55.6/-77.0	-20.2/3.4/13.8	-20.7/6.6/7.2	-0.5/0.0/-0.2	-5.5/-4.2/-26.6	4.4/-1.6/-24.0
θ_2 [°]	36.4/75.5/45.9	16.3/90.0/10.1	80.1/89.4/82.5	89.8/90.0/90.0	88.4/88.9/86.1	90.0/89.4/82.9

Front Spar	1 (Root)	2	3	4	5	6	7	8 (Tip)
t [mm]	5.1/1.4/3.0	0.4/0.3/0.3	0.3/0.3/0.3	0.3/0.3/0.3	0.3/0.3/0.3	0.3/0.3/0.3	0.3/0.3/0.3	0.3/0.3/0.3
θ_1 [°]	20.8/-11.1/1.7	20.7/-61.1/-30.6	10.5/-23.8/-70.4	-40.1/-3.1/-68.9	9.8/-1.8/0.4	-0.5/-2.5/-37.2	-0.3/-6.3/-62.3	0.8/1.4/1.7
θ_2 [°]	90.0/86.5/90.0	90.0/5.3/27.3	90.0/10.8/5.7	90.0/90.0/7.9	61.3/68.4/73.1	77.1/80.9/78.4	74.8/79.8/72.6	83.0/81.1/78.4

Rear Spar	1 (Root)	2	3	4 (Tip)
t [mm]	3.9/1.9/3.3	0.3/0.3/0.3	0.3/0.3/0.3	0.3/0.3/0.4
θ_1 [°]	-26.7/-28.6/-11.3	5.8/-26.9/-61.0	-9.6/-72.8/-69.9	-19.1/-18.2/-11.7
θ_2 [°]	72.9/35.6/45.0	90.0/40.7/40.9	43.3/58.4/75.5	89.3/88.2/86.3

the span which is extremely non desirable, as they create weak points. This means that, alternative methods of manufacturing would be needed or the addition of constraints to make sure the ply angles would be the same across the groups from the different wingbox components.

6 CONCLUSIONS

A alternative wingbox structural solution for the AR5 wing was obtained, leading to an expected reduction of weight of about 50% while maintaining its structural rigidity, with a 1.5 safety factor. It is also important to note that, with further refinement of the computational model, both geometrically, with a more detailed mesh, and in terms of material characterization, with closer to reality mechanical properties, this methodology and high-fidelity framework proved to be a powerful tool to create optimal structural solutions.

One of the major drawbacks from the results presented in this work is the fact that it is not feasible to manufacture the optimal wingbox by traditional means, such as manual layup, since there is a large disparities between ply angles of adjacent DV groups. However, to manufacture this optimal solution, tow-steering technology could be used. The other major limitation from the obtained results is the fact that no buckling constraints were included.

As future work, it is suggested the implementation in this framework of constraints that impose continuity of the DV groups' ply angles across the wingbox components (each skin and spar), as well as a new or improved material constitutive law to substitute the smeared approach, that would allow more control of the layup as well as the use of buckling constraints.

ACKNOWLEDGEMENTS

The authors would like to thank Tekever for supporting the production of this article by offering all the needed data to successfully produce the analyses here shown. This work was supported by FCT, through IDMEC, under LAETA, project UIDB/50022/2020.

REFERENCES

[1] S. Gallardo-Saavedra, L. Hernández-Callejo, and O. Duque-Perez. Technological review of the instrumentation used in aerial thermographic inspection of photovoltaic plants. *Renewable and Sustainable Energy Reviews*, 93:566–579, 2018. ISSN 1364-0321. doi:10.1016/j.rser.2018.05.027.

[2] D. C. Tsouros, S. Bibi, and P. G. Sarigiannidis. A review on uav-based applications for precision agriculture. *Information*, 10(11), 2019. ISSN 2078-2489. doi:10.3390/info10110349.

[3] H. Yao, R. Qin, and X. Chen. Unmanned aerial vehicle for remote sensing applications—a review. *Remote Sensing*, 11(12), 2019. ISSN 2072-4292. doi:10.3390/rs11121443.

[4] P. Cohn, A. Green, M. Langstaff, and M. Roller. Commercial drones are here: The future of unmanned aerial systems. *McKinsey & Company*, 2017. URL `https://www.mckinsey.com/industries/travel-logistics-and-infrastructure/our-insights/commercial-drones-are-here-the-future-of-unmanned-aerial-systems`.

[5] Tekever official website - AR5, May 2023. URL `https://www.tekever.com/models/ar5/`.

[6] D. Grose. Reengineering the aircraft design process. In *5th Symposium on Multidisciplinary Analysis and Optimization*, Panama City Beach, FL, U.S.A., September 1994.

[7] K. K. Rumayshah, A. Prayoga, and M. A. Moelyadi. Design of high altitude long endurance uav: Structural analysis of composite wing using finite element method. *Journal of Physics: Conference Series*, 1005(1):012025, April 2018. doi:10.1088/1742-6596/1005/1/012025.

[8] G. J. Kennedy and J. R. Martins. A parallel finite-element framework for large-scale gradient-based design optimization of high-performance structures. *Finite Elements in Analysis and Design*, 87:56–73, 2014. doi:10.1016/j.finel.2014.04.011.

[9] J. N. Reddy. *Mechanics of laminated composite plates and shells: theory and analysis*. CRC Press, 2003.

[10] T. J. Hughes and F. Brezzi. On drilling degrees of freedom. *Computer Methods in Applied Mechanics and Engineering*, 72(1):105–121, 1989. doi:10.1016/0045-7825(89)90124-2.

[11] D. Fox and J. Simo. A drill rotation formulation for geometrically exact shells. *Computer Methods in Applied Mechanics and Engineering*, 98(3):329–343, 1992. doi:10.1016/0045-7825(92)90002-2.

[12] J. R. R. A. Martins, G. Kennedy, and G. K. Kenway. High aspect ratio wing design: Optimal aerostructural tradeoffs for the next generation of materials. In *52nd Aerospace Sciences Meeting*, National Harbor, Maryland, January 2014. doi:10.2514/6.2014-0596.

[13] G. Kennedy and J. R. R. A. Martins. A comparison of metallic and composite aircraft wings using aerostructural design optimization. In *12th AIAA Aviation Technology, Integration, and Operations (ATIO) Conference and 14th AIAA/ISSMO Multidisciplinary Analysis and Optimization Conference*, Indianapolis, Indiana.

[14] G. K. W. Kenway and J. R. R. A. Martins. Multipoint high-fidelity aerostructural optimization of a transport aircraft configuration. *Journal of Aircraft*, 51(1):144–160, 2014. doi:10.2514/1.C032150.

[15] N. Werter and R. De Breuker. A novel dynamic aeroelastic framework for aeroelastic tailoring and structural optimisation. *Composite Structures*, 158:369–386, 2016. doi:10.1016/j.compstruct.2016.09.044.

[16] N. Wu, G. Kenway, C. A. Mader, J. Jasa, and J. R. R. A. Martins. pyoptsparse: A python framework for large-scale constrained nonlinear optimization of sparse systems. *Journal of Open Source Software*, 5(54):2564, 2020. doi:10.21105/joss.02564.

[17] J. R. R. A. Martins and A. Ning. *Engineering Design Optimization*. Cambridge University Press, 2021. doi:10.1017/9781108980647.

[18] Z. Lyu, Z. Xu, and J. R. Martins. Benchmarking optimization algorithms for wing aerodynamic design optimization. In *The 8th International Conference on Computational Fluid Dynamics*, Chengdu, Sichuan, China, July 2014. ICCFD8-2014-0203.

[19] L. Zhou, J. Huang, Z. Gao, and W. Zhang. Three-dimensional aerodynamic/stealth optimization based on adjoint sensitivity analysis for scattering problem. *AIAA Journal*, 58(6):2702–2715, 2020. doi:10.2514/1.J059136.

[20] G. Yang and A. D. Ronch. Aerodynamic shape optimisation of benchmark problems using su2. In *2018 AIAA/ASCE/AHS/ASC Structures, Structural Dynamics, and Materials Conference*, Kissimmee, Florida, January 2018. doi:10.2514/6.2018-0412.

[21] I. Gibert Martínez, F. Afonso, S. Rodrigues, and F. Lau. A sequential approach for aerodynamic shape optimization with topology optimization of airfoils. *Mathematical and Computational Applications*, 26(2), 2021. ISSN 2297-8747. doi:10.3390/mca26020034.

[22] A. El Ibrahim, S. Abdulkerim, and I. Göv. Aero structural optimization for sailplane wing in preliminary design. *Journal of Advances in Technology and Engineering Research*, 4, 02 2018. doi:10.20474/jater-4.1.5.

[23] R. T. Haftka. Simultaneous analysis and design. *AIAA Journal*, 23(7):1099–1103, 1985. doi:10.2514/3.9043.

[24] S. Sethi, A. Striz, S. Sethi, and A. Striz. On using the kreisselmeier-steinhauser function in simultaneous analysis and design. In *38th Structures, Structural Dynamics, and Materials Conference*, Kissimmee, FL, U.S.A., April 1997. doi:10.2514/6.1997-1289.